Dynamical Analysis of Tropopause Folding Events in the Coastal Region of Antarctica

MASASHI KOHMA,[a] MASATOSHI MIZUKOSHI,[a] AND KAORU SATO[a]

[a] *Department of Earth and Planetary Science, Graduate School of Science, The University of Tokyo, Tokyo, Japan*

(Manuscript received 3 November 2021, in final form 15 March 2022)

ABSTRACT: Tropopause folding events (TFs) are characterized by the rapid and deep descent of the tropopause and are considered to play a significant role in mass exchange between the stratosphere and troposphere. In the present study, TFs occurring in the Antarctic coastal region were examined using the ERA5 dataset. First, the climatological distribution of TF frequency in the extratropics of the Southern Hemisphere was examined. Similar to results from previous studies, TFs were found to often occur along the coast of Antarctica, which is located more than 1000 km south of the maximum of the eddy kinetic energy of synoptic-scale disturbances. This result suggests that the climatological pattern of frequency of TFs in the southern high latitudes cannot be explained only by the geographical distribution of storm tracks. Next, a composite analysis of TFs at Syowa Station was performed. When the negative anomaly of the tropopause height was greatest, strong Q-vector divergence and downwelling were observed in the vicinity of the TF locations. The distribution of Q vectors is related to a local westerly jet and strengthening of the frontal structure associated with meridionally contracted synoptic-scale disturbances. The roles of the topography of the Antarctic Plateau and the radiative cooling on the surface of the continent during the contraction of the disturbances are also discussed based on ray-tracing theory.

KEYWORDS: Antarctica; Fronts; Stratosphere-troposphere coupling; Tropopause

1. Introduction

The tropopause is the boundary between the troposphere and stratosphere. Conventionally, the tropopause is defined by the temperature lapse rate (WMO 1957). Because a sharp change in the potential vorticity (PV) is observed near the tropopause and PV is materially conserved under frictionless and adiabatic conditions, the definition of tropopause based on the PV (the "dynamical tropopause") is often used in studies on the extratropical tropopause and synoptic-scale disturbances. In particular, the dynamical tropopause is useful for examining the tropopause in the polar winter region, where the lapse-rate-based tropopause is often undetected due to the low temperature in the lower stratosphere (e.g., Zängl and Hoinka 2001).

The tropopause height has a temporal variability over a wide range of time scales, from less than 1 day to more than several years (e.g., Keyser and Shapiro 1986; Hoskins et al. 1985; Wirth 2000; Randel et al. 2007; Son et al. 2007; Grise et al. 2010; Kohma and Sato 2014; 2019). One of the most prominent phenomena in the tropopause variability is tropopause folding events (TFs), which are characterized by the rapid and deep descent of the tropopause and a folding structure (Bjerknes and Palmen 1937). Hereinafter, TFs are defined simply as deep intrusion of stratospheric air into the troposphere although several previous studies (e.g., Sprenger et al. 2003; Škerlak et al. 2015) distinguish TFs and stratospheric intrusion based on whether multiple tropopause levels are detected. It is well known that TFs accompany the intrusion of stratospheric air into the troposphere and play an important role in mass exchange between the stratosphere and troposphere (Holton et al. 1995; Stohl et al. 2003; Gettelman et al. 2011; Škerlak et al. 2014; Greenslade et al. 2017; Akritidis et al. 2018). Several observational studies with aircraft and radar measurements reported that turbulence is stronger around TFs (e.g., Cho et al. 1999; Kennedy and Shapiro 1975; Reid and Vaughan 2004; Schäfler et al. 2021). Recently, Söder et al. (2021) demonstrated the vertical profiles of turbulent energy dissipation rates from high-resolution velocity measurements on descending balloon during two typical TFs.

Extratropical TFs are often associated with upper-tropospheric frontogenesis. Keyser and Shapiro (1986) reviewed the dynamics of extratropical TFs associated with the upper-tropospheric front system: according to the Sawyer–Eliassen equation (e.g., Hoskins and James 2014, ch. 15), geostrophic forcing drives cross-frontal ageostrophic/secondary circulation in the vicinity of an upper-tropospheric jet streak. That is, thermodynamically direct circulation (i.e., cold air sinks, warm air rises) is driven in the jet entrance while indirect circulation is driven in the jet exit. These circulation results in development of an upper-tropospheric front and deep descent of the tropopause.

Denotes content that is immediately available upon publication as open access.

Mizukoshi's current affiliation: Japanese Meteorological Agency, Tokyo, Japan.

Corresponding author: Masashi Kohma, kohmasa@eps.s.u-tokyo.ac.jp

DOI: 10.1175/JCLI-D-21-0858.1

To examine the climatological geographical distribution of TFs, high-resolution data are required because the horizontal scales of TFs in the cross-frontal direction can be less than 100 km (Shapiro 1976). Because such data were not available in the early 1990s, Ebel et al. (1996) proposed a method for detection of TF occurrence using Q-vector divergence as a measure of downwelling. Elbern et al. (1998) proposed an indicator for TFs by combining Q-vector divergence and PV and showed that the local maximum of frequency of TFs is located along the Antarctic coast, especially the coast of East Antarctica. In recent studies, the global distribution of TFs has been investigated using the PV distribution of reanalysis data (e.g., Škerlak et al. 2015; Sprenger et al. 2003; Akritidis et al. 2021). Sprenger et al. (2003) developed a three-dimensional labeling algorithm that examines whether an air mass with a stratospheric PV value is connected to the stratosphere. By using their algorithm, geometrically isolated PV anomalies, which is associated with nonconservative processes in the troposphere or cutoff of stratospheric air, can be distinguished from TFs. Škerlak et al. (2015) introduced a backward trajectory calculation into Sprenger et al.'s algorithm to ensure that high PV air parcels do not come from the surface. Using reanalysis data over 34 years, they showed that there are hotspots of deep TFs on the coast of Antarctica in June–August (JJA) and west Australia during JJA and on the east coast of North America during December–February (DJF). Note that stratosphere-to-troposphere mass flux is enhanced in austral winter around 65°S, which corresponds to the coast of Antarctica (Sprenger et al. 2003; Škerlak et al. 2015; Boothe and Homeyer 2017). Thus, it is considered that the TFs along the coast of Antarctica likely play a primary role in stratosphere and troposphere exchange in the extratropics.

It is well known that the Antarctic troposphere contains unique atmospheric flows, including katabatic winds (e.g., Parish and Bromwich 1987) and a persistent easterly low-level jet surrounding the Antarctic plateau (e.g., Fulton et al. 2017). These characteristic flows come from the steep topography of the Antarctic continent and strong radiative cooling on the surface of the continent. In addition, synoptic-scale disturbances and mesoscale phenomena embedded in them can be modulated by such background winds, leading unique dynamics of TF formation in the Antarctic.

Only a few previous studies have focused on the TFs occurring along the Antarctic coastal region. Alexander et al. (2013) examined the frequency of TFs at Davis Station (69°S, 78°E) based on 2-yr observations with radiosondes, ozonesondes, a very high-frequency (VHF) radar, and reanalysis data. They showed that the seasonal cycle of the number of TFs has a broad maximum in June–October, which is similar to results from reanalysis data (e.g., Sprenger et al. 2003). Mihalikova et al. (2012) examined a TF event occurring at the Swedish/Finnish stations WASA/Aboa (73°S, 13.5°W) in boreal summer using radar observations and numerical simulation with a horizontal resolution of 2 km. However, to date, the dynamics of TFs in the Antarctic region has not been studied adequately.

In the present study, the TFs in the Antarctic were examined using the ERA5 dataset to clarify the uniqueness of TFs in the Antarctic. First, the geographical distribution of the frequency of TFs in the extratropical region of the Southern Hemisphere was investigated. Then, we focused on the TFs occurring near Syowa Station (69.0°S, 40.5°E) and performed a composite analysis to clarify the dynamics of TFs. The downward motion associated with the TFs was examined based on the diagnosis of the Q vector in the quasigeostrophic system. Finally, we evaluated the mechanism behind the frequent occurrence of TFs along the coast of Antarctica based on ray-tracing theory and discussed the role of the Antarctic Plateau.

This paper is organized as follows. A description of data and methods for determining tropopause heights and TFs is given in section 2. In section 3, the results of the composite analysis of TFs are presented. The dynamics of meridional contraction of synoptic-scale disturbances is also discussed. Section 4 provides a summary and concluding remarks.

2. Data and methods

a. ERA5

In the present study, ERA5 data (Hersbach et al. 2020) from 2000 to 2019 were used. The forecast model used in the ERA5 is based on Integrated Forecast System Cycle 41r2, and the assimilation system is the incremental 4D-Var with 12-h assimilation window. The data product used here has 37 pressure levels from 1000 to 1 hPa including 250, 300, 350, 400, 450, 500, 550, 600, 650, and 700 hPa, a grid resolution of 0.5° × 0.5° in longitude and latitude, and a time interval of 3 h. This study uses three-dimensional wind, temperature, specific humidity, geopotential, and potential vorticity.

b. Definition of the dynamical tropopause and TF

The present study used the PV-based definition of tropopause, namely isosurfaces of −2 PVU (1 PVU = 10^{-6} K m^2 kg^{-1} s^{-1}) in the Southern Hemisphere, which is widely used for the definition of extratropical tropopause. As previous studies (e.g., Sprenger et al. 2003; Škerlak et al. 2015) pointed out, it is necessary to distinguish TFs from isolated PV anomalies associated with stratospheric cutoffs or tropospheric nonconservative processes including diabatic heating and surface friction in the troposphere. In the present study, the following procedure was used to examine whether an air mass is connected in three dimensions to the stratosphere (Fig. 1):

1) At the top of the reanalysis data (p_0 = 1 hPa), regard all grid points as stratospheric air mass.
2) Move down to the next pressure level (p_i).
3) For each grid point (x, y, p_i) where $|\mathrm{PV}(x, y, p_i)| >$ 2 PVU, extract a 2° × 2° longitude–latitude domain centered on (x, y) at the upper pressure level p_{i-1}.
4) If a stratospheric air mass exists within the domain, regard (x, y, p_i) as a stratospheric air mass.
5) Repeat steps 2 through 4 until p_i reaches the bottom (1000 hPa).

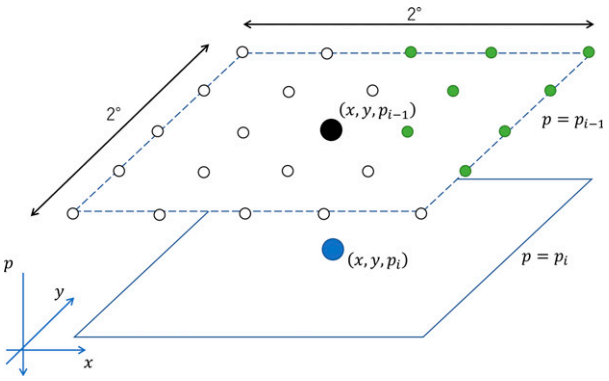

FIG. 1. Schematic diagram for examining connection to the stratospheric air mass. A blue closed circle indicates a grid point (x, y, p_i) where $|\mathrm{PV}(x, y, p_i)| > 2$ PVU. Open circles and green closed circles indicate grid points within the 2° × 2° longitude–latitude domain centered on (x, y, p_{i-1}) (a black closed circle). Green closed circles indicate the stratospheric air mass.

For analysis of TFs, the $z_{\mathrm{PV}}(x, y, t)$ is defined as the lowest level of the stratospheric air mass at each horizontal grid point. In the present study, the TF was defined by the condition in which the deviation of z_{PV} from the time mean z_{PV} is less than −4 km. This is because extratropical TFs are caused by upper-tropospheric jet-front systems accompanied with (synoptic scale) transient disturbances (Keyser and Shapiro 1986). In addition, the criterion for specific humidity is applied to distinguish between TFs and PV anomalies produced diabatically in the troposphere. Similar to z_{PV}, z_Q is defined as the lowest level of dry air mass connected to the stratosphere. A threshold for stratospheric dry air mass is chosen to be a specific humidity of less than 0.1 g kg^{-1}, which is the same as that used in previous studies (e.g., Sprenger et al. 2003; Škerlak et al. 2015). In summary, TFs in the present analysis are identified by the following criteria:

1) z_{PV} is more than 4 km below the 30-day running mean z_{PV}.
2) z_Q is more than 4 km below the 30-day running mean z_{PV}.

Note that the threshold for z_{PV} corresponds to the medium and deep TFs in the classification of Sprenger et al. (2003) and Škerlak et al. (2015) at high southern latitudes.

Before proceeding to the analysis, the differences in the algorithm of detecting tropopause and TFs between the present study and previous studies are briefly discussed. One difference concerns the distinction between TFs and PV anomalies due to nonconservative processes. Škerlak et al. (2015) proposed a sophisticated algorithm for detecting tropopause folds, in which back trajectory calculation for each stratospheric air candidate is performed to confirm that the air mass does not come from the surface. They pointed out that strong radiative cooling on the surface of the Antarctic continent will lead to PV generation, which can cause erroneous detection of TFs [Fig. 4b of Škerlak et al. (2015)]. Because the present study focuses on the TFs occurring along the coastal region of Antarctica, such a situation is unlikely to affect the main results of the present study. Note that the frequency of TFs over the Antarctic continent is quite small compared to that in the coastal region of Antarctica and lower latitudes, as shown in section 3a. Another difference concerns the definition of TFs. In previous studies (e.g., Sprenger et al. 2003; Škerlak et al. 2015), TFs are defined as coexisting multiple dynamical tropopause levels. However, TFs in this study are defined as the deep intrusion of stratospheric air mass and do not necessarily have a folding structure, although the threshold of the depth of the intrusion is the same as in the previous studies. Thus, the occurrence frequency of TFs in this study can be slightly higher than that in the previous studies. It should be noted that multiple tropopause levels are observed in most of the TFs in the coastal region of Antarctica, and that the composite of the dynamical tropopause during TFs occurring at Syowa Station has a folding structure, as will be shown in section 3b. The other difference is the algorithm used to confirm the connection with stratospheric PV. Whereas in previous studies only adjacent grid points were used to confirm a connection to the stratospheric PV, the present algorithm uses a 2° × 2° longitude–latitude domain (Fig. 1). This reduces the cutoff of the PV isosurface caused by large-amplitude gravity waves. Previous studies showed that orographic gravity waves are excited due to strong surface winds blowing across the coast of Antarctica (e.g., Watanabe et al. 2006; Tomikawa et al. 2015; Vignon et al. 2020). Figure 2 shows a typical example of

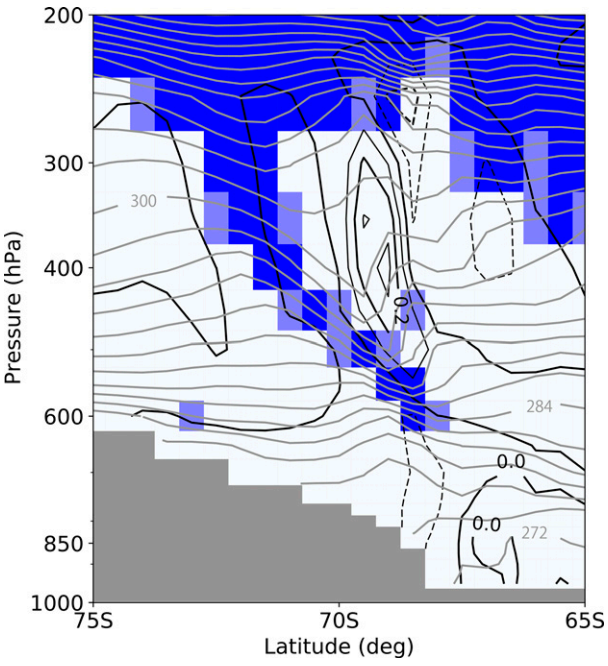

FIG. 2. A latitude–height section of PV (color), vertical wind (black contours), and potential temperature (gray contours) at 0900 UTC 16 Nov 2004 at 43°E. Solid (broken) black contours indicate upward (downward) motion. The contour intervals for vertical wind and potential temperature are 0.1 m s^{-1} and 5 K, respectively. Blue (cyan) color indicates air mass with |PV| 2.0 (1.5) PVU.

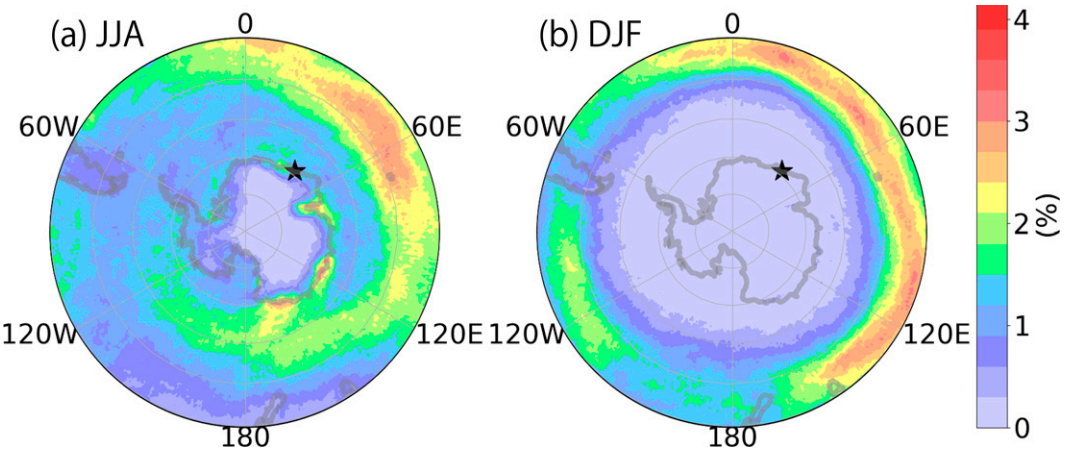

FIG. 3. Spatial distributions of the frequency of TFs in (a) JJA and (b) DJF. The elevation higher than 2.5 km is denoted by thick gray contours. The stars mark the location of Syowa Station. The latitude circles start from 40°S with an interval of 10°.

the cutoff of the 2-PVU isosurface due to large-amplitude gravity waves at 0900 UTC 16 November 2004. The 2-PVU isosurface shows a folding structure along the front, while there are grid points with $|PV| > 2$ PVU at (69.5°S, 500 hPa), (69.0°S, 550 hPa), and (68.5°S, 550–600 hPa) that are not directly connected to the stratospheric air mass. The 2-PVU contour line is broken at 70°S, where upward winds exceed 0.3 m s^{-1}. The phase front of the vertical wind is aligned with the coast of Antarctica, and strong northward winds are observed at the surface level (not shown), indicating that the strong vertical wind disturbances are associated with orographic gravity waves (e.g., Tomikawa et al. 2015). In the present algorithm, the region comprising four grid points with $|PV| > 2$ PVU at (69.5°S, 500 hPa), (69.0°S, 550 hPa), (68.5°S, 550 hPa), and (68.5°S, 550 hPa) is regarded as the stratospheric air mass. Note that although linear (inertia) gravity waves have zero PV (e.g., Vallis 2017), they can induce numerical errors in calculating PV. The frequency of resolved gravity waves in ERA5 is large compared to other reanalyses with lower horizontal resolution, although the amplitude in modern reanalysis data, including ERA5, is still small compared to observations (Podglajen et al. 2020). Furthermore, orographic waves are frequently generated in the vicinity of the steep topography of the Antarctic Plateau, which is beyond the scope of the present study. In summary, due to the differences in the algorithm examining connection of stratospheric air mass, the frequency of TFs in the present analysis will be larger than those from previous studies (e.g., Škerlak et al. 2015; Akritidis et al. 2021), which is discussed in section 3a.

3. Results

a. Geographical distribution of tropopause folds

Figure 3 shows the spatial distribution of TF frequency south of 40°S in JJA and DJF. In both seasons, a frequency maximum is observed in the latitude range of 40°–50°S. This is in agreement with results based on CAMS reanalysis and MERRA-2 by Akritidis et al. (2021). South of 50°S, there is a frequency maximum along the coast of Antarctica in JJA, whereas the frequency in DJF is quite small compared to that at lower latitudes. It is also found that the frequency of TFs is higher in the coastal region of East Antarctica than in West Antarctica.

The large frequency of the TFs along the coastal region of Antarctica during austral winter has been reported by previous studies (e.g., Sprenger et al. 2003), and this is the focus of our study. Note that the frequency of medium and deep TFs based on MERRA-2 and CAMS reanalysis results (Akritidis et al. 2021), which have similar horizontal resolution (0.625 × 0.5° and 0.7° × 0.7°, respectively), is smaller than the present result. This is likely due to the difference in the algorithms used to confirm the connection to the stratospheric PV, as discussed in section 2b.

To examine the relation with geographical distributions of the upper-tropospheric jet and storm tracks, the eddy kinetic energy per unit mass (EKE) at 300 hPa was calculated, where EKE is defined as $(1/2)(u'^2 + v'^2)$, u (v) is the zonal (meridional) wind, and the prime symbol denotes the high-pass filtered component with a period shorter than 10 days (e.g., Inatsu et al. 2003). The horizontal wind speeds at 300 hPa are also shown in Fig. 4. It is found that the maxima of EKE are located in the Atlantic and Indian Oceans in JJA, whereas the EKE distribution has a nearly zonally symmetric pattern in DJF. The geographical distributions of EKE in JJA and DJF are similar to those of the horizontal wind speeds (contours in Fig. 4) and the variance of relative vorticity at 250 hPa presented in previous studies (e.g., Hoskins and Hodges 2005). In both seasons, the latitudinal band where the maximum of TF frequency is observed (40°–50°S) coincides with the latitude band of the upper-tropospheric jet and maximum EKE. In contrast, in JJA the jet maximum or EKE maximum is not found in the vicinity of the coast of Antarctica, where the local maximum of TF frequency is observed. Thus, the climatological distributions of the upper-tropospheric jet and storm tracks do not fully explain the frequent occurrence of TFs in the Antarctic region. This result suggests that the Antarctic continent might play some role in the formation of TFs.

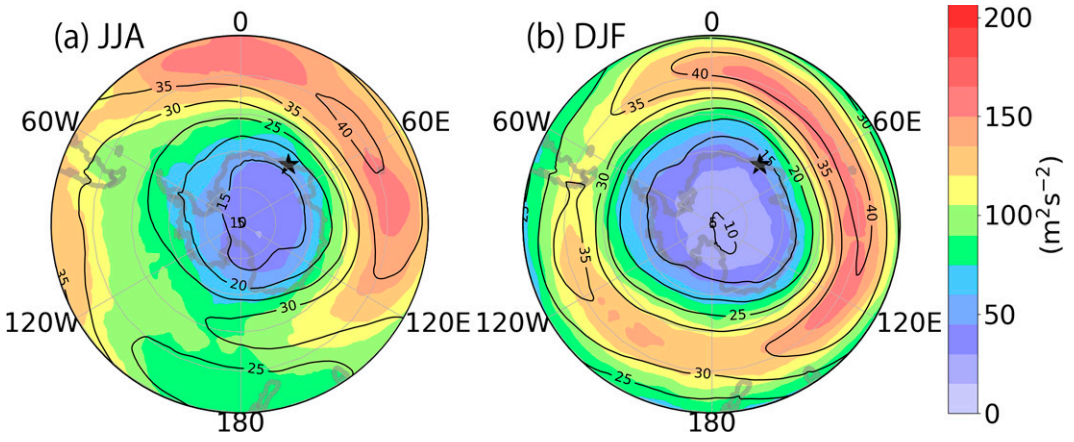

FIG. 4. As in Fig. 3, but for eddy kinetic energy (color) and horizontal wind speed at 300 hPa (black contour). The contour interval is 5 m s^{-1}.

The atmospheric flows unique to the Antarctic region including katabatic winds are those strongly influenced by the topography of Antarctica. For example, the direction of the katabatic winds is mainly determined by the sloping topography, the negative buoyancy associated with surface radiative cooling, Coriolis force, and surface friction (Ball 1960). Thus, it is suggested that the structure of the TFs can be affected by the steep topography of the edge of Antarctica. To explore this possibility, the orientation of the TF axis, determined in the following manner, was examined (Fig. 5). The TF center is defined as the center of gravity of the grid points with $|PV| > 2$ PVU in a 20° × 10° longitude–latitude box. The orientation of the TF axis is defined as the direction of the TF center at an altitude of 5 km relative to the TF center at an altitude of 4 km. To exclude large PV values due to radiative cooling on the surface, areas with an elevation higher than 2.5 km were excluded from the calculation of the TF center. The orientation of the axis was classified into four groups: northwest (NW), northeast (NE), southwest (SW), and southeast (SE). The NE group represents the case where the angle of the vector from the TF center at 5 km to the TF center at 4 km, measured clockwise from the north, is from 0° to less than 90°; conversely, the SE group represents the case where the angle vector over this distance is from 90° to 180°. Similarly, the SW (NW) group represents the case where the angle vector over this distance is from 180° to 270° (from 270° to 360°).

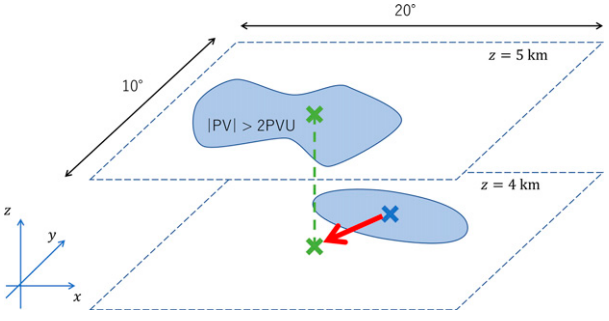

FIG. 5. Schematic diagram showing the orientation of the TF axis. Cyan-colored area indicates the region where $|PV(x, y, p_i)| > 2$ PVU. The green (blue) cross indicates the center of TFs at $z = 5$ (4) km. The red arrow indicates the orientation of the TF axis.

Figures 6b–e show the spatial distribution of the TF frequency for each orientation of the TF axis. Overall, the frequency of TFs with SE and SW directions is large compared to that with NE and NW directions. In particular, the frequency of SE or SW direction TFs is large in the regions where the Antarctic continent is on the SE or SW side, respectively. For example, the frequency of the SE group is large on the east side of the coast at the Ross Sea and Amery Ice shelf compared to the west, whereas the SW group is more frequently observed on the west side. Thus, the orientation of the TF axis is almost parallel to the slope of the Antarctic continent. This result supports the hypothesis that the presence of the Antarctic continent plays an important role in the formation of TFs along the Antarctic coast.

b. *Composite analyses of tropopause fold events*

Next, we performed a composite analysis for the TFs at Syowa Station (69.0°S, 40.5°E) to examine the dynamics of TFs occurring along the coast of Antarctica. In the present composite analysis, we suppose that the first day of a particular TF event should be at least 3 days apart from the last day of the preceding event. As a result, from 2000 to 2019, 120 TF events were identified at Syowa Station. Figure 7 shows number of TFs for each month. The number of TF events at Syowa Station reaches a maximum during austral winter, which is also observed in Fig. 3. In the composite analysis, the reference time $t = 0$ h for each TF event is chosen as the time when the tropopause height is lowest. Here, a high-pass filter with a cutoff period of 10 days is used to extract eddy components associated with transient (synoptic-scale) disturbances, as before. Note that the orientation of the TF axis for most TFs at Syowa Station belongs to the SE group, as shown in section 3a (Fig. 3). We confirmed that the following results do not change significantly when only orientation of the TF axis with the SE direction are analyzed.

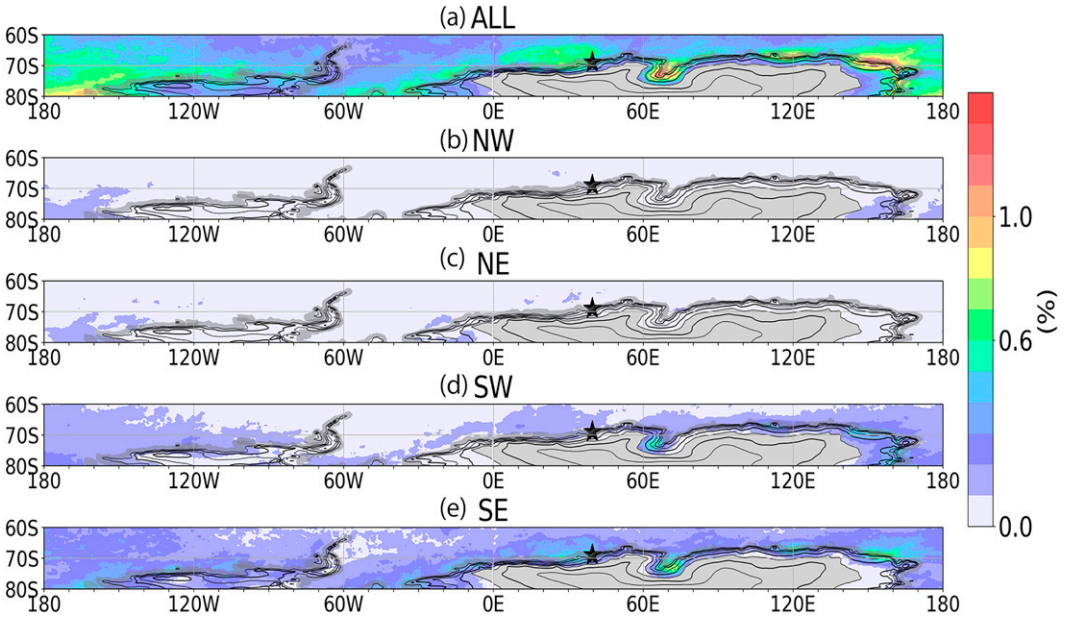

FIG. 6. (a) Spatial distributions of the TF frequency in the latitude range of 60°–80°S. The contours indicate elevation. Gray indicates the regions where the elevation exceeds 2.5 km. The contour interval is 0.5 km. (b)–(e) As in (a), but for the frequency of the orientation of the TF axis from the (b) NW, (c) NE, (d) SW, and (e) SE directions.

Figures 8a–c show composite horizontal maps of z_{PV} anomalies at $t = -12$, 0, and 12 h. Before the lowest tropopause was observed at Syowa Station ($t = -12$ h), negative z_{PV} anomalies of at most 1 km are observed west of Syowa Station. Subsequently, statistically significant negative z_{PV} anomalies are observed between 35° and 55°E along the coast of Antarctica at $t = 0$ h (Fig. 8b). It is interesting to note that the average orientation of the TF axis (the purple arrow in Fig. 8b) crosses the coastline of Antarctica, which is consistent with results shown in Fig. 6. Zonal wind and geopotential height anomalies at 500 hPa are shown in Figs. 8d–f. At $t = -12$ h, synoptic-scale negative geopotential height anomalies are observed around 70°S, 50°E, while a positive anomaly is observed NW of Syowa Station. The negative geopotential height anomaly strengthens and shifts slightly to the west when TFs are observed at Syowa Station. The positive geopotential height anomaly over the sea moves eastward. Between these geopotential height anomalies, the meridional gradient of geopotential height strengthens, and westerly jet anomalies are observed along the coast of Antarctica. Accordingly, a jet streak develops to the north of Syowa Station.

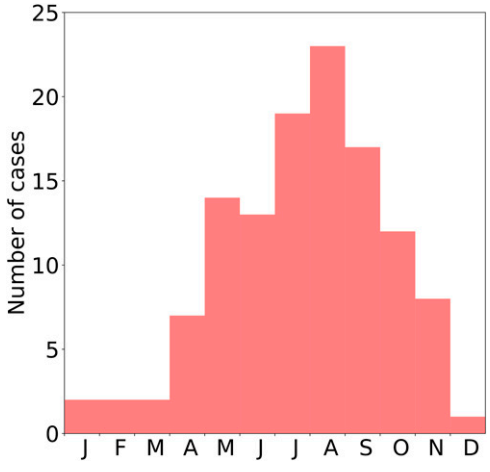

Fig. 7. Number of TF events at Syowa Station for each month, 2000–19. A TF event is defined as a period in which TFs are continuously observed at Syowa Station, and the first day of a TF event is at least 3 days away from the last day of the preceding TF event.

To investigate the frontogenesis during TF formation, composite maps of potential temperature θ and anomalies of horizontal gradient of potential temperature $|\nabla_H\theta|$ $[= \sqrt{(\partial\theta/\partial x)^2 + (\partial\theta/\partial y)^2}]$ at 500 hPa were made (Figs. 8g–i). At all times shown in the plots, the meridional gradient θ is large at 68°–75°S, which is consistent with the climatologically strong radiative cooling at the Antarctic surface (e.g., Fulton et al. 2017). The maximum of the anomaly of $|\nabla_H\theta|$ is observed at $t = 0$ h on the south flank of the westerly anomaly at the same level. Thus, similar to TFs occurring in other latitudinal regions (Keyser and Shapiro 1986), most of the TFs at Syowa Station are accompanied by the jet front system.

Figures 8j–l show composites of anomalies of vertical wind w at 500 hPa. At $t = 0$ h, significant downward motions are observed along the coast of Antarctica at 27°–43°E, which corresponds to the entrance region of the local westerly jet (Fig. 8e). The largest negative anomalies of vertical wind are observed at Syowa Station, with a magnitude of

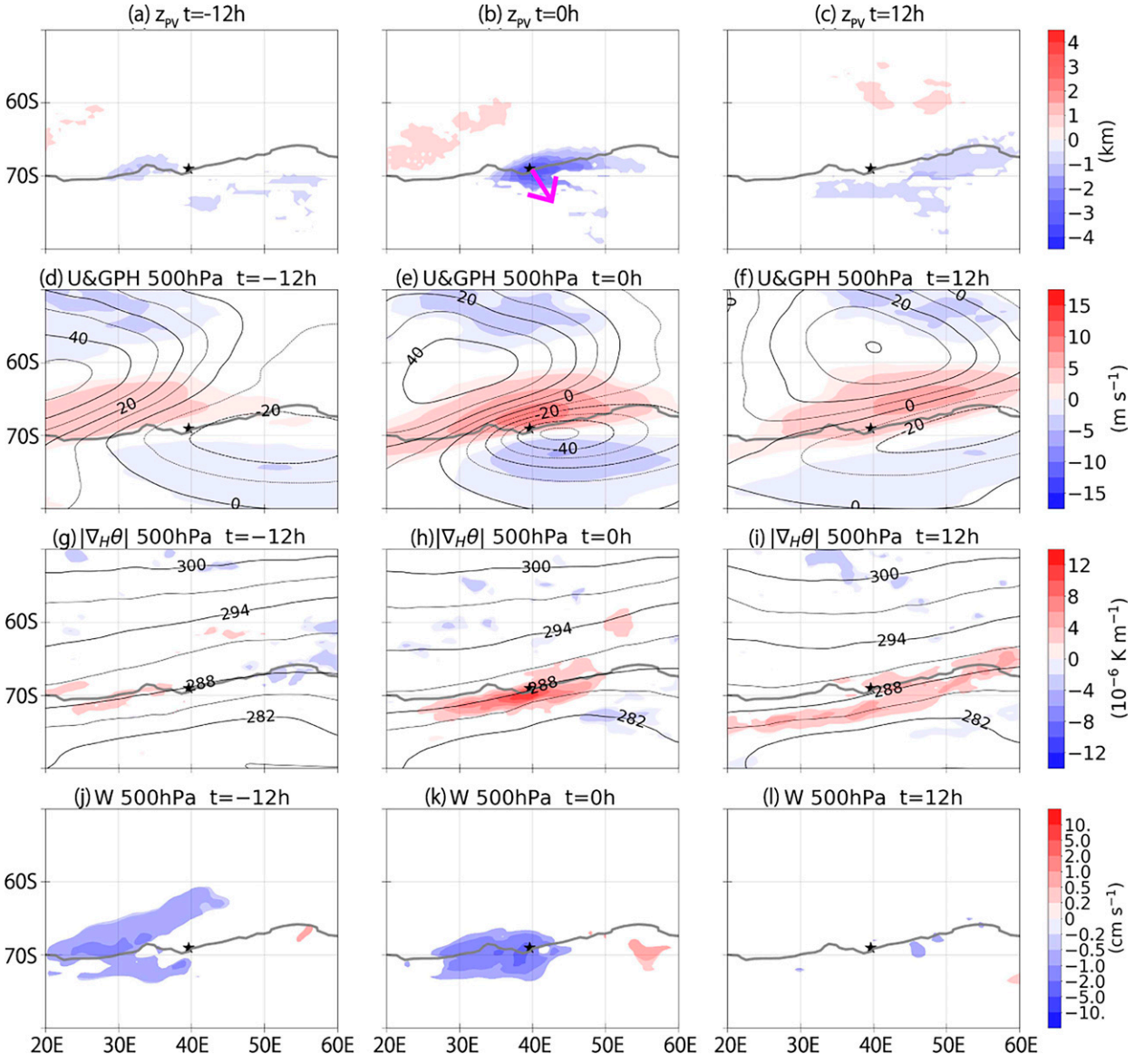

FIG. 8. (a)–(c) Composites of anomalies of z_{PV} at t = (a) −12, (b) 0, and (c) 12 h. Only areas with a 95% confidence level for the two-sided t test are colored. Gray thick contours indicate the coast of Antarctica. Stars indicate the location of Syowa Station (69.0°S, 39.5°E). The mean orientation of TF axis is indicated by the purple arrow in (b). (d)–(f) As in (a)–(c), but for anomalies of zonal wind (color) and geopotential heights (contours) at 500 hPa. The contour interval is 10 m. (g)–(i) As in (a)–(c), but for potential temperature (contours) and anomalies of $|\nabla_H\theta|$ (color) at 500 hPa. The contour interval is 3 K. (j)–(l) As in (a)–(c), but for anomalies of vertical wind at 500 hPa.

2 cm s^{-1}. At t = 12 h, the whole system moves eastward compared to t = 0 h, and no significant vertical flow is observed around Syowa Station. Figure 9 shows latitude–height sections of anomalies of w at t = −12, 0, and 12 h at 39.5°E, the longitude closest to Syowa Station. The folding structure is associated with downward flow anomaly extending from the lower stratosphere to the Antarctic continent. Note that the composite of the dynamical tropopause shows a folding structure even though the present algorithm does not use the criterion for multiple detection of the tropopause (e.g., Sprenger et al. 2003).

To examine the relation between downward motion and jet-front system, the Q vector in the quasigeostrophic system was computed following Holton and Hakim (2012):

$$\mathbf{Q} = -\frac{R}{p}\left(\frac{\partial \mathbf{v}_g}{\partial x}\cdot\nabla_H T,\ \frac{\partial \mathbf{v}_g}{\partial y}\cdot\nabla_H T\right)$$
$$= -\frac{R}{p}\left(-\frac{\partial v_g}{\partial y}\frac{\partial T}{\partial x}+\frac{\partial v_g}{\partial x}\frac{\partial T}{\partial y},\ \frac{\partial u_g}{\partial y}\frac{\partial T}{\partial x}-\frac{\partial u_g}{\partial x}\frac{\partial T}{\partial y}\right),$$

where $\mathbf{v}_g = (u_g, v_g)$ is the geostrophic wind vector, T is temperature, p is pressure, and R is the gas constant for dry air. The

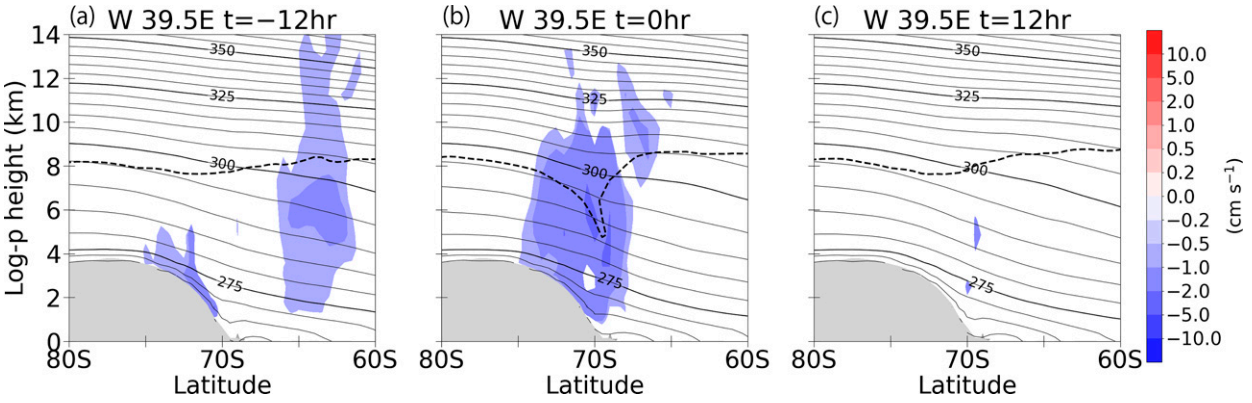

FIG. 9. Composites of height–latitude sections of potential temperature (contour) and anomalies of vertical winds (color) at 39.5°E at t = (a) −12, (b) 0, and (c) +12 h. The contour interval is 5 K. The regions with a statistical confidence level higher than 95% are colored. Black dotted curves indicate composites of the dynamical tropopause heights.

operator ∇_H represents the horizontal gradient. The vertical pressure velocity ω is diagnosed by omega equation if nonconservative terms are neglected:

$$\sigma\nabla_H^2\omega + f_0^2\frac{\partial^2\omega}{\partial p^2} = -2\nabla_H\cdot\mathbf{Q} + f_0\beta\frac{\partial v_g}{\partial p} + \frac{R}{p}\nabla_H^2 J, \qquad (2)$$

where $f_0 = 2\Omega\sin\phi_0$ is the Coriolis parameter at latitude ϕ_0, $\beta = 2\Omega\cos\phi_0/a$ represents the latitudinal change of the Coriolis parameter, $\sigma = -RT_0p^{-1}d\ln\theta_0/dp$ is the static stability of the reference atmosphere, and J represents the heating rate due to nonconservative processes (e.g., diabatic processes). The second term on the right-hand side of Eq. (2) is small compared to the first term in most situations. We confirmed that the contribution of diabatic heating [the third term on right-hand side of Eq. (2)] is one order of magnitude smaller than divergence of the Q vector [the first term on right-hand side of Eq. (2)] during TF formation (not shown). Because the differential operator on the left-hand side of Eq. (2) is elliptical, the divergence (convergence) of the Q vector will result in downward (upward) motion. Figure 10a shows composites of anomalies of the Q vector and its divergence at t = 0 h. It can be seen that a large Q vector is heading NE around Syowa Station, and Q-vector divergence is observed SW of Syowa Station (i.e., south of the entrance of the jet streak). The Q-vector divergence is almost coincident with the regions where the significant downward motion and lowering of the tropopause are observed. Thus, the dynamics of TFs at Syowa Station can be understood, at least qualitatively, in the framework of the quasigeostrophic equation system.

It should be noted that the Q vector shown in Fig. 10a includes effects of the upper-level jet front system as well as those of background fields of temperature and geostrophic winds. In particular, a climatological meridional gradient of temperature exists along the coastline due to the strong radiative cooling on the continent (Figs. 8g–i). To examine roles of background fields together with transient eddies, the Q vector was decomposed as follows:

$$\begin{aligned}
\mathbf{Q} &= \mathbf{Q}_{bb} + \mathbf{Q}_{aa} + \mathbf{Q}_{ab} + \mathbf{Q}_{ba},\\
\mathbf{Q}_{bb} &= -\frac{R}{p}\left(\frac{\partial\tilde{\mathbf{v}}_g}{\partial x}\cdot\nabla_H\tilde{T}, \frac{\partial\tilde{\mathbf{v}}_g}{\partial y}\cdot\nabla_H\tilde{T}\right),\\
\mathbf{Q}_{aa} &= -\frac{R}{p}\left(\frac{\partial\mathbf{v}_g'}{\partial x}\nabla_H T', \frac{\partial\mathbf{v}_g'}{\partial y}\cdot\nabla_H T'\right),\\
\mathbf{Q}_{ab} &= -\frac{R}{p}\left(\frac{\partial\mathbf{v}_g'}{\partial x}\cdot\nabla_H\tilde{T}, \frac{\partial\mathbf{v}_g'}{\partial y}\cdot\nabla_H\tilde{T}\right),\\
\mathbf{Q}_{ba} &= -\frac{R}{p}\left(\frac{\partial\tilde{\mathbf{v}}_g}{\partial x}\cdot\nabla_H T', \frac{\partial\tilde{\mathbf{v}}_g}{\partial y}\cdot\nabla_H T'\right), \qquad (3)
\end{aligned}$$

where $\tilde{T}$ and $\tilde{\mathbf{v}}_g$ are background fields of geostrophic wind vector and temperature, respectively. The background fields were extracted using a low-pass filter with a cutoff period of 10 days. The term $\mathbf{Q}_{ab}$ represents interaction between the transient geostrophic wind anomaly and the background temperature gradient; $\mathbf{Q}_{ba}$ denotes interaction between the background geostrophic wind and the temperature gradient anomaly. Figures 10b–d show composite maps of anomalies of $\mathbf{Q}_{aa}$, $\mathbf{Q}_{ba}$, and $\mathbf{Q}_{ab}$ at 500 hPa. Note that the anomaly of $\mathbf{Q}_{bb}$ is exactly zero. It can be seen that $\mathbf{Q}_{aa}$ contributes significantly to the distribution of $\mathbf{Q}$ and $\nabla_H\cdot\mathbf{Q}$ around significant negative anomalies of z_{PV}. While $\mathbf{Q}_{ba}$ is divergent west of Syowa Station, $\mathbf{Q}_{ab}$ does not have large values near Syowa Station. In summary, the distribution of $\mathbf{Q}$ vectors during TFs is explained primarily by the local westerly jet and the frontal structure associated with synoptic-scale disturbances, whereas the contribution of the background meridional temperature gradient is secondary.

c. *Mechanism of shrinkage of disturbances in the meridional direction*

In this section, we discuss why TFs occur so frequently in the Antarctic coastal zone. First, we examine the time evolution of synoptic-scale disturbances a few days before TFs occur at Syowa Station. Figure 11 shows composites of geopotential height anomalies at 700 hPa. Twenty-four hours before the lowest tropopause heights are observed (Figs. 11d–h), a

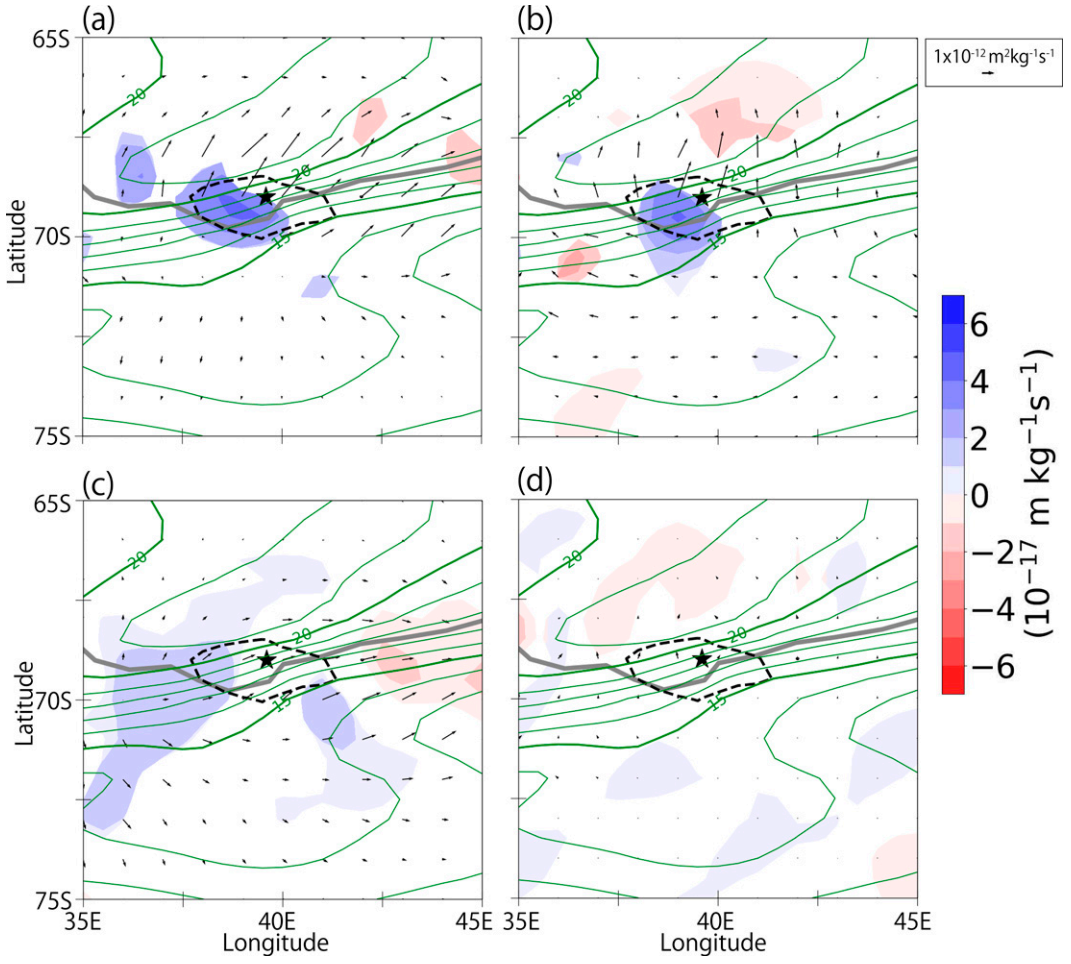

FIG. 10. (a) Composites of anomalies of the Q vector (arrows) and its divergence (color) together with wind speed (green contours) at 500 hPa at $t = 0$ h. The contour interval is 1 m s^{-1}. Regions surrounded by a broken curve are locations where the anomaly of the tropopause height is lower than 3 km. (b)–(d) As in (a), but for (b) $\mathbf{Q}_{aa}$, (c) $\mathbf{Q}_{ba}$, and (d) $\mathbf{Q}_{ab}$.

NE–SW tilt of negative geopotential height anomalies is observed. From 12 h before (Figs. 11f–h), the meridional gradient of the geopotential height anomaly increases around Syowa Station. This is accompanied by the strengthening of the local westerly jet and frontal structure shown in section 3b, resulting in strong downwelling and descent in the tropopause. These results suggest that to elucidate the reason for the frequent occurrence of TFs near the Antarctic coast, the dynamics of increasing meridional gradient of geopotential heights (i.e., the dynamics of meridional-scale contraction of the disturbance) needs to be clarified.

To consider the mechanism of disturbance contraction in the meridional direction, the tendency of the meridional wavenumber was evaluated in the framework of the Wentzel–Kramers–Brillouin–Jeffreys (WKBJ) approximation. Consider Rossby waves propagating in the steady and zonally uniform background field. The background wind field is assumed to be $[\mathbf{u}] = ([u], 0, 0)$. The (local) dispersion relation of Rossby waves is given as follows (e.g., Andrews et al. 1987):

$$\omega = [u]k - \frac{k\dfrac{\partial [q_g]}{\partial y}}{k^2 + l^2 + \dfrac{f_0^2}{N^2}\left(m^2 + \dfrac{1}{4H^2}\right)}, \tag{4}$$

where ω is the observed angular frequency; k, l, and m are zonal, meridional, and vertical wavenumbers, respectively; $N^2 = N^2(z)$ is the reference profile of buoyancy frequency squared; H is the density scale height; and $[q_g]$ represents the background quasigeostrophic PV (QGPV). The background QGPV is given by

$$[q_g] = f - \frac{\partial^2 [\psi]}{\partial y^2} + \frac{1}{\rho_0}\frac{\partial}{\partial z}\left(\frac{f_0^2}{N^2}\rho_0 \frac{\partial [\psi]}{\partial z}\right), \tag{5}$$

where $[\psi]$ is a streamfunction of the background geostrophic winds and $\rho_0 = \rho_0(z)$ is a reference profile of the density. The meridional group velocity is given by

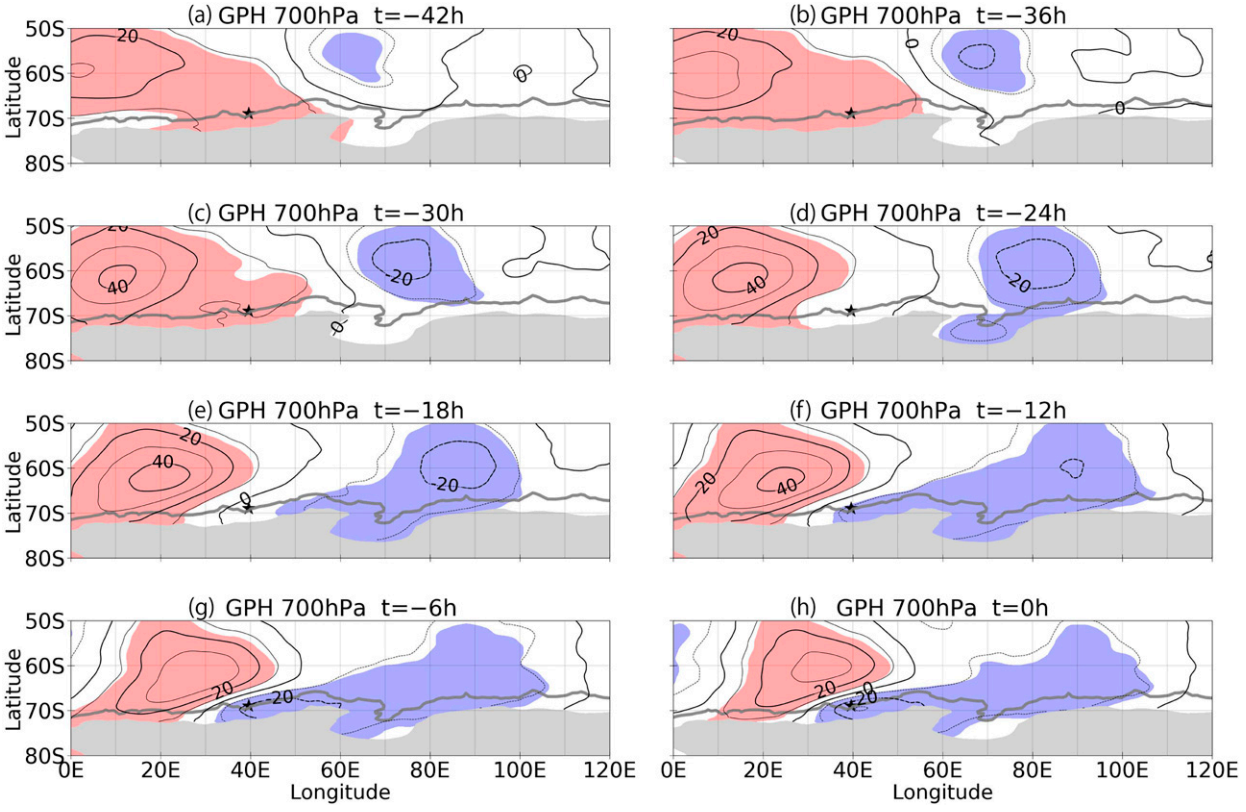

FIG. 11. Composites of geopotential height anomaly at 700 hPa at t = (a) −42, (b) −36, (c) −30, (d) −24, (e) −16, (f) −12, (g) −6, and (h) 0 h. The regions with a statistical confidence level higher than 95% are colored. Gray thick curves indicate the coast of Antarctica. The region where the elevation is higher than 2.5 km is shaded gray.

$$c_{gy} \equiv \frac{\partial \omega}{\partial l} = \frac{2kl\,\dfrac{\partial [q_g]}{\partial y}}{\left[k^2 + l^2 + \dfrac{f_0^2}{N^2}\left(m^2 + \dfrac{1}{4H^2}\right)\right]^2}. \tag{6}$$

Because geopotential anomalies exhibit a SW–NE tilt before TFs form (Figs. 11d–f), k and l have signs opposite to each other (i.e., $kl < 0$). Because $\partial[q_g]/\partial y$ is usually positive, disturbances causing TFs at Syowa Station have a southward group velocity. According to ray-tracing theory, when the background field is steady and zonally uniform, ω and k are constant along the ray, namely wave packet propagation. Thus, the eastward phase velocity c_{px}, which is defined by

$$c_{px} \equiv \frac{\omega}{k} = [u] - \frac{\dfrac{\partial [q_g]}{\partial y}}{k^2 + l^2 + \dfrac{f_0^2}{N^2}\left(m^2 + \dfrac{1}{4H^2}\right)}, \tag{7}$$

is also conserved along the wave propagation. In the following, we separately consider the change in meridional wavenumber l of southward propagating (synoptic-scale) disturbances due to the meridional variation of the background fields of u and $\partial[q_g]/\partial y$. Here, the change of vertical wavenumber m is assumed to be negligible because the vertical structure of the synoptic-scale disturbance does not significantly change before and during TFs (not shown).

Figures 12a and 12b show latitude–height sections of zonal winds at 40°E for JJA and DJF, respectively. In both seasons, easterly winds prevail near the slope of the Antarctic Plateau, while westerly winds are dominant at lower latitudes. Previous studies have shown that the low-level easterly winds surround the Antarctic Plateau all year round and can be explained as a balanced flow due to the topography of the continent and strong radiative cooling at the surface (Fulton et al. 2017). To keep c_{px} constant for wave packets propagating southward in the cyclonic shear ($\overline{u}_y > 0$), the magnitude of l^2 $\{= \partial[q_g]/\partial y/([u] - c_{\mathrm{px}}) - k^2 - (f_0^2/N^2)[m^2 + 1/(4H^2)]\}$ must increase because of $\partial[q_g]/\partial y > 0$ and constant k if $[u] - c_{px} > 0$ [Eq. (7)].

Figures 12c and 12d show the QGPV for JJA and DJF, respectively. To calculate $[q_g]$, we used $f_0 = 2\Omega\sin(70°\mathrm{S})$, $N^2 = 10^{-4}\ \mathrm{s}^{-2}$, and $H = 7$ km. It was found that the QGPVs are negatively maximized along the slope of Antarctica. This is due to the strong radiative cooling at the surface of Antarctica (e.g., Fulton et al. 2017). Accordingly, $\partial[q_g]/\partial y$ values are maximized off the coast of Antarctica. The large $\partial[q_g]/\partial y$ extends away from the coast (e.g., to 65°S) at an altitude of 3 km in JJA. Similar to the zonal wind, the

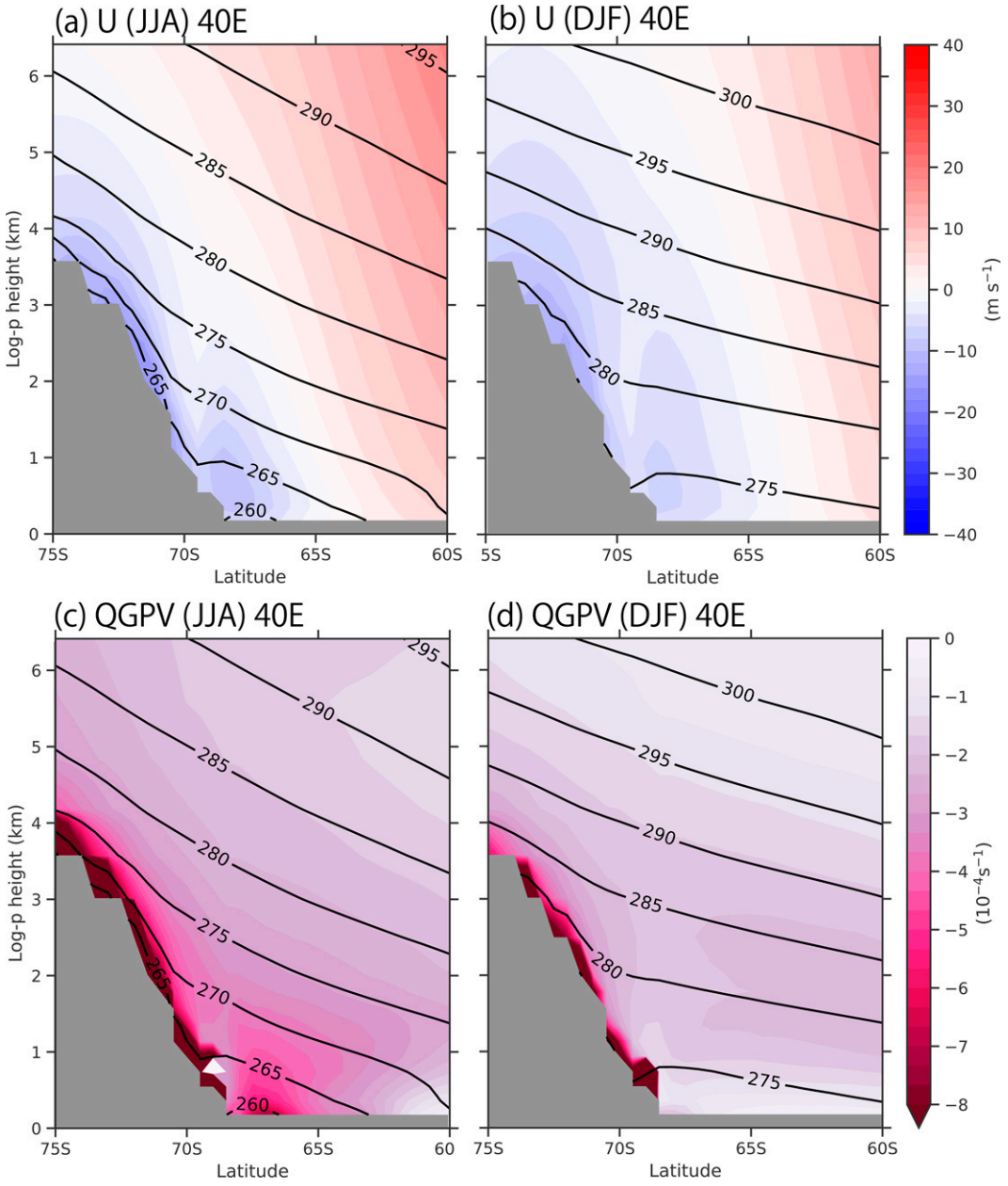

FIG. 12. Latitude–height sections of zonal wind (color) and potential temperature (contours) at 40°E averaged over (a) JJA and (b) DJF. The contour interval is 5 K. (c),(d) As in (a),(b), but for QGPV.

magnitude of l for wave packets with southward group velocity needs to increase near the Antarctic coastal region to keep c_{px} constant. It is interesting to note that $\partial[q_g]/\partial y$ in the vicinity of Antarctica is larger in JJA than in DJF, which indicates that synoptic-scale disturbances are more likely to contract in the coastal region in winter than in summer. Thus, the large occurrence frequency of TFs in the coastal region in austral winter (Fig. 7) may be explained by the seasonality of $\partial[q_g]/\partial y$ around the Antarctic coast together with that of activity of synoptic-scale disturbances (Hoskins and Hodges 2005).

In summary, from the ray tracing theory, it is considered that the meridional wavenumber increases during southward propagation of the wave packet due to background fields of zonal wind and QGPV associated with the topography of Antarctica and radiative cooling at the surface. Thus, the meridional scale of the system becomes small, and the meridional gradient of geopotential height anomalies has a structure extending west–east. As a result, the westerly jet and frontal structure are enhanced along the coast of Antarctica, resulting in strong downwelling and descent in tropopause heights. Therefore, the steep topography of the Antarctic Plateau and

radiative cooling at the continent surface play primary roles in the frequent occurrence of TFs along the coast of Antarctica. This is consistent with the fact that TFs more frequently occur in East Antarctica than in West Antarctica (Fig. 3a) because the flank of East Antarctica is steeper. It should be noted that although the slope of the Antarctic continent is not parallel to the meridional direction, the same conclusion can be obtained by rotating the system properly.

4. Summary and concluding remarks

Using 20 years of reanalysis data, we examined the dynamics of TFs occurring in the coastal region of Antarctica. The dynamics of TFs in the Antarctic region has not been fully investigated, although previous studies pointed out that TFs are frequently observed along the Antarctic coast in austral winter. The obtained results can be summarized as follows:

- In austral winter, TFs often occur along the coast of Antarctica, especially along the East Antarctic coast. It is important to note that the coast of Antarctica is located far south of the maximum of the eddy kinetic energy of synoptic-scale eddies. Thus, the climatological distribution of upper-tropospheric jet and storm tracks does not fully explain the large frequency of TFs along the coast of Antarctica.
- From the composite analyses of TFs occurring at Syowa Station, it is found that the TFs occur in relation to the Q-vector divergence and the resulting strong downwelling. The distribution of Q vectors is explained by the local westerly jet and strengthening of the frontal structure associated with synoptic-scale disturbances.
- The contraction of the meridional scale of synoptic-scale disturbances off the coast of Antarctica during TFs was evaluated using ray tracing theory. The contraction can be attributed to the background zonal wind and the PV (QGPV) around the coast of Antarctica, which is produced by the steep topography of the Antarctic Plateau and radiative cooling at the surface.
- In austral summer, a local maximum of TF frequency is hardly observed along the Antarctic coast. This is likely because the background meridional gradient of QGPV around the coast of Antarctica is weaker in summer than in winter, and thus the contraction of the synoptic-scale disturbances rarely occurs in summer.

The present discussion on the contraction of the synoptic-scale disturbances is based on WKBJ approximation. The WKBJ approximation is, strictly speaking, valid when spatial scales of the background state are much larger than the wavelength of the disturbances of interest. In the present case, the spatial scale of the background PV fields in the coastal region may be comparable to that of the synoptic-scale waves (Figs. 12c,d). Nevertheless, it is known that the WKBJ theory provides qualitative guidance on the time evolution of (local) wavenumber even when the scale separation between the wavelength and the spatial scale of background fields is small (e.g., Vallis 2017). Thus, the tendency of meridional wavenumber estimated under the WKBJ approximation by the present study shows, at least qualitatively, that the Antarctic Plateau has a major role in the occurrence of TFs in the coastal region.

TFs are considered to accompany small-scale turbulent processes, which affects PV generation and efficiency of irreversible mixing (Keyser and Shapiro 1986; Holton et al. 1995). To perform further investigation of turbulent processes associated with TFs, we plan to make an analysis for the turbulence energy dissipation rates and eddy diffusion coefficients using VHF clear-air Doppler radar and operational radiosonde observations at Syowa Station (Sato et al. 2014; Kohma et al. 2019).

Acknowledgments. The present study was supported by the Japan Society for the Promotion of Science, KAKENHI Grant JP19K14791, and the Japan Science and Technology Agency, CREST Grant JPMJCR1663. We thank Keiichi Ishioka for helpful comments on this work. The authors acknowledge three anonymous reviewers for greatly helping us to improve this manuscript.

Data availability statement. ERA5 data are available from the Copernicus Climate Change Service Climate Data Store (https://cds.climate.copernicus.eu/cdsapp#!/dataset/reanalysis-era5-pressure-levels?tab=overview).

REFERENCES

Akritidis, D., and Coauthors, 2018: A deep stratosphere-to-troposphere ozone transport event over Europe simulated in CAMS global and regional forecast systems: Analysis and evaluation. *Atmos. Chem. Phys.*, **18**, 15 515–15 534, https://doi.org/10.5194/acp-18-15515-2018.

——, A. Pozzer, J. Flemming, A. Inness, and P. Zanis, 2021: A global climatology of tropopause folds in CAMS and MERRA-2 reanalyses. *J. Geophys. Res. Atmos.*, **126**, e2020JD034115, https://doi.org/10.1029/2020JD034115.

Alexander, S. P., D. J. Murphy, and A. R. Klekociuk, 2013: High resolution VHF radar measurements of tropopause structure and variability at Davis, Antarctica (69°S, 78°E). *Atmos. Chem. Phys.*, **13**, 3121–3132, https://doi.org/10.5194/acp-13-3121-2013.

Andrews, D. G., J. R. Holton, and C. B. Leovy, 1987: *Middle Atmosphere Dynamics.* Academic Press, 489 pp.

Ball, F. K., 1960: Winds on the ice slopes of Antarctica. *Proceedings of the Symposium on Antarctic Meteorology, Melbourne 1959*, Pergamon Press, 9–16.

Bjerknes, J. P., and E. Palmen, 1937: Investigations of selected European cyclones by means of serial ascents. *Geofys. Publ.*, **12**, 1–62.

Boothe, A. C., and C. R. Homeyer, 2017: Global large-scale stratosphere–troposphere exchange in modern reanalyses. *Atmos. Chem. Phys.*, **17**, 5537–5559, https://doi.org/10.5194/acp-17-5537-2017.

Cho, J. Y. N., and Coauthors, 1999: Observations of convective and dynamical instabilities in tropopause folds and their contribution to stratosphere–troposphere exchange. *J. Geophys. Res.*, **104**, 21 549–21 568, https://doi.org/10.1029/1999JD900430.

Ebel, A., H. Elbern, J. Hendricks, and R. Meyer, 1996: Stratosphere–troposphere exchange and its impact on the

structure of the lower stratosphere. *J. Geomag. Geoelectr.*, **48**, 135–144, https://doi.org/10.5636/jgg.48.135.

Elbern, H., J. Hendricks, and A. Ebel, 1998: A climatology of tropopause folds by global analyses. *Theor. Appl. Climatol.*, **59**, 181–200, https://doi.org/10.1007/s007040050023.

Fulton, S. R., W. H. Schubert, Z. Q. Chen, and P. E. Ciesielski, 2017: A dynamical explanation of the topographically bound easterly low-level jet surrounding Antarctica. *J. Geophys. Res. Atmos.*, **122**, 12 635–12 652, https://doi.org/10.1002/2017JD027192.

Gettelman, A., P. Hoor, L. L. Pan, W. J. Randel, M. I. Hegglin, and T. Birner, 2011: The extratropical upper troposphere and lower stratosphere. *Rev. Geophys.*, **49**, RG3003, https://doi.org/10.1029/2011RG000355.

Greenslade, J. W., S. P. Alexander, R. Schofield, J. A. Fisher, and A. K. Klekociuk, 2017: Stratospheric ozone intrusion events and their impacts on tropospheric ozone in the Southern Hemisphere. *Atmos. Chem. Phys.*, **17**, 10 269–10 290, https://doi.org/10.5194/acp-17-10269-2017.

Grise, K. M., D. W. J. Thompson, and T. Birner, 2010: A global survey of static stability in the stratosphere and upper troposphere. *J. Climate*, **23**, 2275–2292, https://doi.org/10.1175/2009JCLI3369.1.

Hersbach, H., and Coauthors, 2020: The ERA5 global reanalysis. *Quart. J. Roy. Meteor. Soc.*, **146**, 1999–2049, https://doi.org/10.1002/qj.3803.

Holton, J. R., and G. J. Hakim, 2012: *An Introduction to Dynamic Meteorology*. 5th ed., Academic Press, 552 pp., https://doi.org/10.1016/C2009-0-63394-8.

——, P. H. Haynes, M. E. McIntyre, A. R. Douglass, R. B. Rood, and L. Pfister, 1995: Stratosphere–troposphere exchange. *Rev. Geophys.*, **33**, 403–439, https://doi.org/10.1029/95RG02097.

Hoskins, B. J., and K. I. Hodges, 2005: A new perspective on Southern Hemisphere storm tracks. *J. Climate*, **18**, 4108–4129, https://doi.org/10.1175/JCLI3570.1.

——, and I. N. James, 2014: *Fluid Dynamics of the Midlatitude Atmosphere*. Wiley Blackwell, 408 pp., https://doi.org/10.1002/9781118526002.

——, M. E. McIntyre, and A. W. Robertson, 1985: On the use and significance of isentropic potential vorticity maps. *Quart. J. Roy. Meteor. Soc.*, **111**, 877–946, https://doi.org/10.1002/qj.49711147002.

Inatsu, M., H. Mukougawa, and S. P. Xie, 2003: Atmospheric response to zonal variations in midlatitude SST: Transient and stationary eddies and their feedback. *J. Climate*, **16**, 3314–3329, https://doi.org/10.1175/1520-0442(2003)016<3314:ARTZVI>2.0.CO;2.

Kennedy, P. J., and M. A. Shapiro, 1975: Energy budget in a clear air turbulence zone as observed by aircraft. *Mon. Wea. Rev.*, **103**, 650–654, https://doi.org/10.1175/1520-0493(1975)103<0650:TEBIAC>2.0.CO;2.

Keyser, D., and M. A. Shapiro, 1986: A review of the structure and dynamics of upper-level frontal zones. *Mon. Wea. Rev.*, **114**, 452–499, https://doi.org/10.1175/1520-0493(1986)114<0452:AROTSA>2.0.CO;2.

Kohma, M., and K. Sato, 2014: Variability of upper tropospheric clouds in the polar region during stratospheric sudden warmings. *J. Geophys. Res. Atmos.*, **119**, 10 100–10 113, https://doi.org/10.1002/2014JD021746.

——, and ——, 2019: A diagnostic equation for tendency of lapse-rate-tropopause heights and its application. *J. Atmos. Sci.*, **76**, 3337–3350, https://doi.org/10.1175/JAS-D-19-0054.1.

——, ——, Y. Tomikawa, K. Nishimura, and T. Sato, 2019: Estimate of turbulent energy dissipation rate from the VHF radar and radiosonde observations in the Antarctic. *J. Geophys. Res. Atmos.*, **124**, 2976–2993, https://doi.org/10.1029/2018JD029521.

Mihalikova, M., S. Kirkwood, J. Arnault, and D. Mikhaylova, 2012: Observation of a tropopause fold by MARA VHF wind-profiler radar and ozonesonde at Wasa, Antarctica: Comparison with ECMWF analysis and a WRF model simulation. *Ann. Geophys.*, **30**, 1411–1421, https://doi.org/10.5194/angeo-30-1411-2012.

Parish, T. R., and D. H. Bromwich, 1987: The surface wind field over the Antarctic ice sheets. *Nature*, **328**, 51–54, https://doi.org/10.1038/328051a0.

Podglajen, A., A. Hertzog, R. Plougonven, and B. Legras, 2020: Lagrangian gravity wave spectra in the lower stratosphere of current (re)analyses. *Atmos. Chem. Phys.*, **20**, 9331–9350, https://doi.org/10.5194/acp-20-9331-2020.

Randel, W. J., D. J. Seidel, and L. L. Pan, 2007: Observational characteristics of double tropopauses. *J. Geophys. Res.*, **112**, D07309, https://doi.org/10.1029/2006JD007904.

Reid, H. J., and G. Vaughan, 2004: Convective mixing in a tropopause fold. *Quart. J. Roy. Meteor. Soc.*, **130**, 1195–1212, https://doi.org/10.1256/qj.03.21.

Sato, K., and Coauthors, 2014: Program of the Antarctic Syowa MST/IS radar (PANSY). *J. Atmos. Sol.-Terr. Phys.*, **118A**, 2–15, https://doi.org/10.1016/j.jastp.2013.08.022.

Schäfler, A., A. Fix, and M. Wirth, 2021: Mixing at the extratropical tropopause as characterized by collocated airborne H_2O and O_3 lidar observations. *Atmos. Chem. Phys.*, **21**, 5217–5234, https://doi.org/10.5194/acp-21-5217-2021.

Shapiro, M. A., 1976: The role of turbulent heat flux in the generation of potential vorticity in the vicinity of upper-level jet stream systems. *Mon. Wea. Rev.*, **104**, 892–906, https://doi.org/10.1175/1520-0493(1976)104<0892:TROTHF>2.0.CO;2.

Škerlak, B., M. Sprenger, and H. Wernli, 2014: A global climatology of stratosphere–troposphere exchange using the ERA-Interim data set from 1979 to 2011. *Atmos. Chem. Phys.*, **14**, 913–937, https://doi.org/10.5194/acp-14-913-2014.

——, ——, S. Pfahl, E. Tyrlis, and H. Wernli, 2015: Tropopause folds in ERA-Interim: Global climatology and relation to extreme weather events. *J. Geophys. Res. Atmos.*, **120**, 4860–4877, https://doi.org/10.1002/2014JD022787.

Söder, J., C. Zülicke, M. Gerding, and F. J. Lübken, 2021: High-resolution observations of turbulence distributions across tropopause folds. *J. Geophys. Res. Atmos.*, **126**, e2020JD033857, https://doi.org/10.1029/2020JD033857.

Son, S. W., S. Lee, and S. B. Feldstein, 2007: Intraseasonal variability of the zonal-mean extratropical tropopause height. *J. Atmos. Sci.*, **64**, 608–620, https://doi.org/10.1175/JAS3855.1.

Sprenger, M., M. C. Maspoli, and H. Wernli, 2003: Tropopause folds and cross-tropopause exchange: A global investigation based upon ECMWF analyses for the time period March 2000 to February 2001. *J. Geophys. Res.*, **108**, 8518, https://doi.org/10.1029/2002JD002587.

Stohl, A., and Coauthors, 2003: Stratosphere–troposphere exchange: A review, and what we have learned from STACCATO. *J. Geophys. Res.*, **108**, 8516, https://doi.org/10.1029/2002JD002490.

Tomikawa, Y., and Coauthors, 2015: Vertical wind disturbances during a strong wind event observed by the PANSY radar at Syowa Station, Antarctica. *Mon. Wea. Rev.*, **143**, 1804–1821, https://doi.org/10.1175/MWR-D-14-00289.1.

Vallis, G. K., 2017: *Atmospheric and Oceanic Fluid Dynamics: Fundamentals and Large-Scale Circulation.* 2nd ed., Cambridge University Press, 946 pp., https://doi.org/10.1017/9781107588417.

Vignon, E., G. Picard, C. Durán-Alarcón, S. P. Alexander, H. Gallée, and A. Berne, 2020: Gravity wave excitation during the coastal transition of an extreme katabatic flow in Antarctica. *J. Atmos. Sci.*, **77**, 1295–1312, https://doi.org/10.1175/JAS-D-19-0264.1.

Watanabe, S., K. Sato, and M. Takahashi, 2006: A general circulation model study of the orographic gravity waves over Antarctica excited by katabatic winds. *J. Geophys. Res.*, **111**, D18104, https://doi.org/10.1029/2005JD006851.

Wirth, V., 2000: Thermal versus dynamical tropopause in upper-tropospheric balanced flow anomalies. *Quart. J. Roy. Meteor. Soc.*, **126**, 299–317, https://doi.org/10.1002/qj.49712656215.

WMO, 1957: Definition of the tropopause. *WMO Bull.*, **6**, 136–140.

Zängl, G., and K. P. Hoinka, 2001: The tropopause in the polar regions. *J. Climate*, **14**, 3117–3139, https://doi.org/10.1175/1520-0442(2001)014<3117:TTITPR>2.0.CO;2.